Research Stay Report: Modelling the Bystander Effect in Proton SFRT

Daniel Puerta Megías
Universidad de Granada
Imperial College London

Contents

1 Introduction

The radiation-induced bystander effects (RIBE) are the non-targetted consequences produced by ionising radiation in non-irradiated cells within or nearby an irradiated volume [Wang et al., 2018]. Cells affected by RIBE only show similar behaviour to those which are irradiated (e.g., cell death, DNA strand breaks and mutations) [Decrock et al., 2017].

These responses have been attributed to the communication from irradiated to non-irradiated cells through contact mechanisms (gap-junction intercellular communication) or soluble excreted factors which travel in the culture medium [Klammer et al., 2015]. The exact signalling agent is not known and a situation-dependant combination of them is more likely. They can be divided in two groups [Marín et al., 2015]:

- Small species, e.g. free radicals, reactive oxygen species (ROS), Ca^{2+} and nitrogen oxide (NO).
- Larger species, e.g. exosomes, cytokines and other proteins[1].

There is evidence of RIBE in many contexts in photon and particle therapy [Mukherjee and Chakraborty, 2019], in experimental settings for partial particle irradiation [Shao et al., 2006] and, in particular, for proton SFRT in some cell lines [Autsavapromporn et al., 2023].

The RIBE are studied in three types of experiments [Shao et al., 2006]: 1) transfer of medium harvested from irradiated cells to non-irradiated cells; 2) co-culture of non-irradiated cells with cells that have previously been irradiated; and 3) irradiation of cells where only a small fraction are irradiated. In the context of spatially fractionated radiotherapy (SFRT), the third situation is the most simular[2].

In this report, we aim to model the RIBE observed in the preliminary results of the experiments performed by our group (see Figure 1).

[1] Exosomes are vesicles secreted by cells enveloped by a lipid membrane [Edgar, 2016]. Cytokines are a broad category of small proteins important in cell signalling [Oppenheim, 2001].

[2] Since cells in the valleys receive some dose, the term "cohort effects" would be more appropriate [Prezado, 2022], but RIBE will be used here.

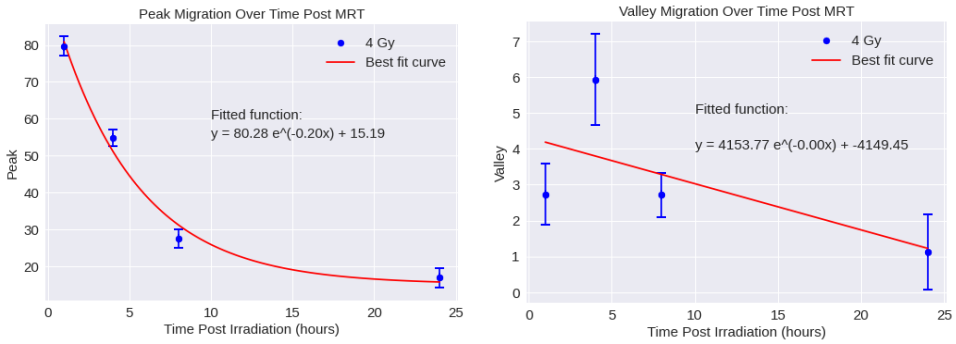

Figure 1: Evolution of DSB over time after proton microbeam irradiation in the peaks (left) and valleys (right). Experiment and image by J. McGarrigle.

In the experiment, FaDu cells were irradiated with 4 and 10 Gy (not shown) using a proton minibeam array of energy 3-30 MeV and size 0.1 x 8 mm^2. The number of double DNA strand breaks (DSB) was analysed over time. The (arguably) sustained damage over long times in the valleys may indicate RIBE. Here, we will focus on the role of small species, specifically H_2O_2 and Ca^{2+}.

2 Generation of ROS in Water Radiolysis

Radiolysis is a fast channel for chemical production that will be present in organisms with water content. The species generated during radiolysis (free radicals and ROS) are part of the RIBE and, due to their quick and ever-present appearance in biological systems, need to be studied.

In Figure 3 we see a graph of the evolution of water radiolysis. Within the first 10^{-12} s, radiation interacts with water breaking the molecule, generating a series of chemical species in the process. From 10^{-12} s to 10^{-6} s, the species diffuse in the volume interacting with each other. At this point, their spatial distribution is heterogeneous, only appearing in the irradiated sections, and their behaviour is best modelled by their individual tracking. From 10^{-6} s up to 1 s after irradiation, the molecules are distributed homogeneously, interacting with the water background and they are best modelled by their concentrations [Masilela, 2023]. Finally, after the first second, biological processes begin and the concentrations of the generated species are modulated.

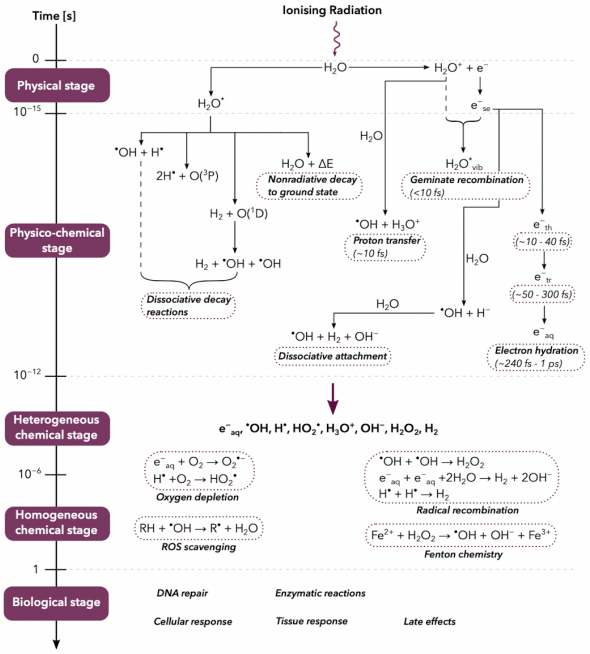

Figure 2: Time evolution of water radiolysis in a biological system. Image retrieved from [Masilela, 2023].

Their production and early transport (up to the heterogeneous chemical stage, less than 10^{-6} s after irradiation) can be simulated with the Monte Carlo code TOPAS [Perl et al., 2012] and its extension TOPAS-nBio [Schuemann et al., 2018]. These physico-chemical simulations are limited to water, but in this report we will extrapolate their results to biological systems using different mathematical models.

In the following, we will explain our simulation, focusing only on H_2O_2 due to its relative stability, chemical similarity to water and strong oxidizing capacity [Prezado, 2022, Masilela, 2023].

2.1 Simulation

We use the set-up presented in [Masilela, 2023]. We simulate one minibeam of 0.4 x 6 mm^2 impinging on a water phantom of 10 x 10 x 100 mm^3. A total of 10^5 protons of 100 MeV were simulated. Particles are transported using the TOPAS packages "g4em-livermore" "g4ion-binarycascade" "g4h-phy_QGSP_BIC_HP" "g4decay" "g4h-elastic_HP" "g4stopping".

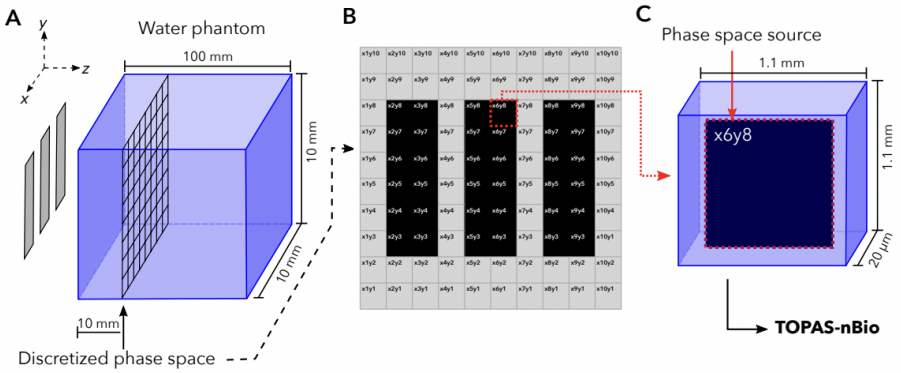

Figure 3: Set-up for TOPAS simulation. Image retrieved from [Masilela, 2023].

At $z = 10$ mm, we divide a surface perpendicular to the z direction into 100 phase space scorers. We record all particles generated during the simulation except neutrons and deuterons whose interactions are not included in TOPAS-nBio.

We then perform a TOPAS-nBio simulation for each of the phase space recorded in a water volume of 1.1 mm x 1.1 mm x 20 μm using the physics

package "g4em-dna_opt2" and the chemistry package "TsEmDNAChemistryExtended". We include the reactions in Figure 4 as indicated in [Ramos-Méndez et al., 2021]. These reactions need to be explicitly defined. For that we used the file "TOPASChemistry_Extended.txt" found in the "nucleusModel" geometry example distributed with the extension.

No.	Reaction			$k(10^{10}$/M/s)[b]
1[a]	$e^-_{aq} + e^-_{aq}$	$\longrightarrow$	$2OH^- + H_2$	0.647
2[a]	$e^-_{aq} + {}^{\bullet}OH$	$\longrightarrow$	OH^-	2.953
3[a]	$e^-_{aq} + H^{\bullet}$	$\longrightarrow$	$OH^- + H_2$	2.652
4[a]	$e^-_{aq} + H_3O$	$\longrightarrow$	$H^{\bullet}$	2.109
5	$e^-_{aq} + H_2O_2$	$\longrightarrow$	$OH^- + {}^{\bullet}OH$	1.405
6[a]	${}^{\bullet}OH + {}^{\bullet}OH$	$\longrightarrow$	H_2O_2	0.475
7[a]	${}^{\bullet}OH + H^{\bullet}$	$\longrightarrow$	No product	1.438
8[a]	$H^{\bullet} + H^{\bullet}$	$\longrightarrow$	H_2	0.503
9[a]	$H_3O + OH^-$	$\longrightarrow$	No product	11.031
10[a]	$H_2 + {}^{\bullet}OH$	$\longrightarrow$	$H^{\bullet}$	0.0045
11	${}^{\bullet}OH + H_2O_2$	$\longrightarrow$	HO_2	0.0023
12	${}^{\bullet}OH + HO_2$	$\longrightarrow$	O_2	1.0
13	${}^{\bullet}OH + O^-_2$	$\longrightarrow$	$O_2 + OH^-$	0.9
14	${}^{\bullet}OH + HO_{-2}$	$\longrightarrow$	$HO_2 + OH^-$	0.9
15	$e^-_{aq} + HO_2$	$\longrightarrow$	HO_{-2}	2.0
16	$e^-_{aq} + O_2$	$\longrightarrow$	O^-_2	1.9
17	$e^-_{aq} + O2^-$	$\longrightarrow$	$OH^- + HO_{-2}$	1.3
18	$H^{\bullet} + H_2O_2$	$\longrightarrow$	${}^{\bullet}OH$	0.01
19	$H^{\bullet} + HO_2$	$\longrightarrow$	H_2O_2	2.0
20	$H^{\bullet} + O_2$	$\longrightarrow$	HO_2	2.0
21[a]	$H^{\bullet} + OH^-$	$\longrightarrow$	e^-_{aq}	0.002
22	$H^{\bullet} + O^-_2$	$\longrightarrow$	HO_{-2}	2.0
23	$H_3O + O^-_2$	$\longrightarrow$	HO_2	3.0
24	$H_3O + HO_{-2}$	$\longrightarrow$	H_2O_2	2.0
25	$HO_2 + HO_2$	$\longrightarrow$	$H_2O_2 + O_2$	0.000076
26	$HO_2 + O^-_2$	$\longrightarrow$	$O2 + HO_{-2}$	0.0085

Notes.

[a] These reactions can occur directly after the pre-chemical stage.

[b] $M = 1$ mol dm^{-3}.

Figure 4: Reactions included in the TOPAS-nBio simulations. Image retrieved from [Masilela, 2023].

We ran the chemical simulation using the step-by-step algorithm up to 1 μs with dynamic time step as explained in [Karamitros et al., 2014]. The scorer pTuple is included to record the position of all molecules at 1 μs.

We used a single minibeam to speed up the simulation. In post-processing, the results are mirrored to -3.2 and 3.2 mm in the x direction, representing a three-minibeam array with center-to-center distance (ctc) of 3.2 mm. The resulting H_2O_2 are shown in Figure 5. The uncertainty of the histrograms is calculated as the standard deviation of the Bernoulli distribution [Salvat, 2018].

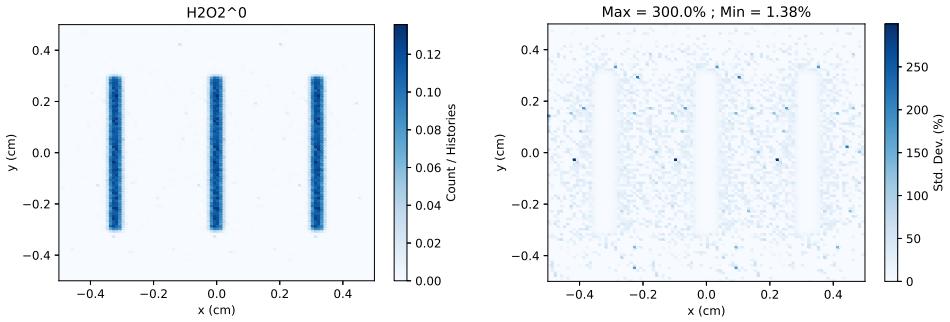

Figure 5: Histogram of H_2O_2 and its uncertainty.

As we can see, the H_2O_2 spatial distribution is marked by that of the minibeams, where most H_2O_2 molecules are in the locations where radiation was aimed at and virtually no H_2O_2 elsewhere.

3 Transport of H_2O_2 After Generation

Our experiments may reflect RIBE in cells at the hour scale while the previous simulation only includes times ≤ 1 μs and water. We will now present an extrapolation of those results to later times and biological systems using two dedicated models.

3.1 Estimating the beginning of the biological stage ($t = 1$ s)

In the homogenous chemical stage, all molecules are evenly distributed in space and the background reactions, described by the master chemical equation, take place. A recent study has implemented the Gillespie algorithm to solve it in TOPAS-nBio [D-Kondo et al., 2023], following the evolution of the molecules produced for 1000 s. In the case of H_2O_2, the concentration increases steadily up to 1 s (Figure 6).

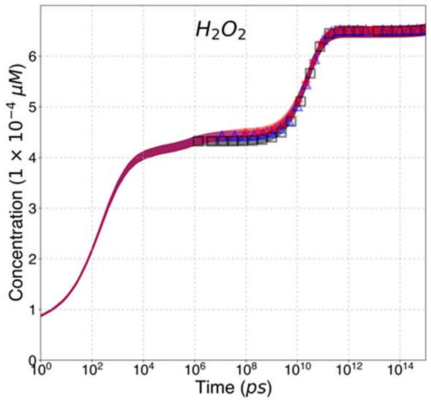

Figure 6: Evolution of H_2O_2 generated in water radiolysis. Image retrieved from [D-Kondo et al., 2023].

For these results to apply, we need to justify that the molecules produced in our simulations will be homogenously distributed from 10^{-6} to 1 s. As seen in Figure 5, H_2O_2 is homogenously distributed within the minibeam peaks and absent elsewhere. We will argue that this behaviour is sustained up to $t = 1$ s by simulating the free diffusion of H_2O_2.

Each H_2O_2 molecule in the phase space will be transported using the

algorithm in TOPAS-nBio [Karamitros et al., 2014]:

$$x(\tau) = x_0 + \sqrt{2D \cdot \tau} \cdot \epsilon_x \tag{1}$$

$$y(\tau) = y_0 + \sqrt{2D \cdot \tau} \cdot \epsilon_y \tag{2}$$

$$z(\tau) = z_0 + \sqrt{2D \cdot \tau} \cdot \epsilon_z \tag{3}$$

where x_0, y_0 and z_0 are the initial coordinates of an individual H_2O_2 molecule, D is the diffusion coefficient of H_2O_2 in water ($D = 2.3 \cdot 10^{-9}$ m^2/s), ϵ_x, ϵ_y and ϵ_z are three uniformly distributed random numbers and τ is the time considered ($\tau = 1$ s in this case).

Our analysis shows that the distributions at 1 μs (Figure 5) and 1 s are similar (Figure 7), indicating that the homogenous chemical stage can occur within the peaks.

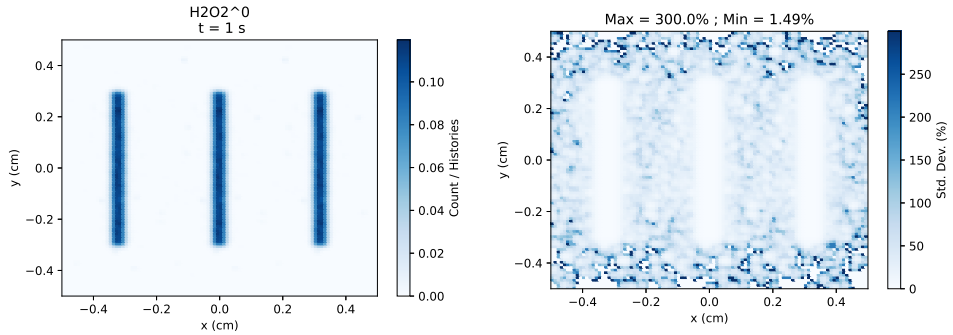

Figure 7: Histogram of H_2O_2 at 1 s and its uncertainty.

In summary, we assume that the H_2O_2 behaviour in [D-Kondo et al., 2023] applies and the spatial distribution of H_2O_2 at 1 μs and 1 s are equal up to an overall factor.

3.2 Diffusion and removal of H_2O_2 in the biological stage

Diffusion without removal cannot be used to study the long term behaviour of H_2O_2 in cells because there are mechanisms for its strict regulation [Möller et al., 2019], thus two models for H_2O_2 transport including scavenging[3] will be introduced:

[3]Both are mathematically equivalent, see Appendix I for proof.

1. Free diffusion following [Karamitros et al., 2014] plus a probability for removal.

2. Numerical solution to Fick's diffusion equation including removal, extending [Zhang et al., 2023] to 2D.

Following [Dal Bello et al., 2020] we will determine the time needed for H_2O_2 to achieve spatial homogeneity in the whole surface.

3.2.1 Model for transport I

We approximate the many removal mechanisms by a pseudo first order global reaction with the background [Shin, 2020]:

$$\frac{d[H_2O_2](\tau)}{d\tau} = -\kappa\,[H_2O_2](\tau) \tag{4}$$

where $[H_2O_2](\tau)$ is the concentration of H_2O_2 at time τ and κ is the global reaction rate constant. Equation 4 is easily solved by $[H_2O_2](\tau) = [H_2O_2](\tau_0)\,e^{-\kappa(\tau-\tau_0)}$, where τ_0 is the time where H_2O_2 is generated, which we set to $\tau_0 = 10^{-6} \sim 0$ s.

In practice, particles are transported using Equations 1-3 and an extra random number ϵ_t is uniformally sampled between 0 and 1. The particle survives if $\epsilon_t < e^{-\kappa\tau}$ and is killed otherwise, representing the probability of a molecule of H_2O_2 being scavenged. We first use $\kappa = 2 \cdot 10^{-1}$, $2 \cdot 10^{-2}$ and $2 \cdot 10^{-3}$ s^{-1} as suggested in [Zhang et al., 2023]. The results can be seen in Figures 8-10. For $\kappa = 2 \cdot 10^{-1}$ s^{-1}, no H_2O_2 survives with this formalism.

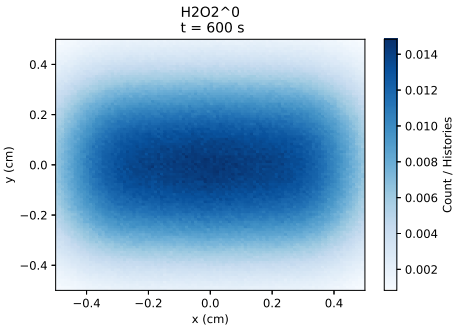

Figure 8: Histogram with pure free diffusion, $\kappa = 0$ s^{-1}.

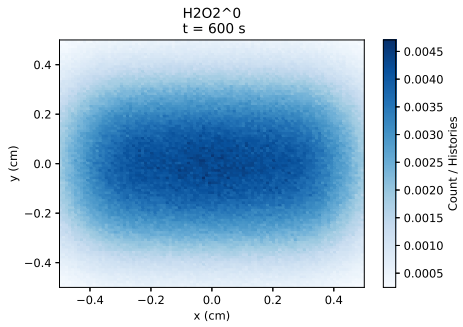

Figure 9: Histogram with $\kappa = 2.3 \cdot 10^{-3}$ s^{-1}.

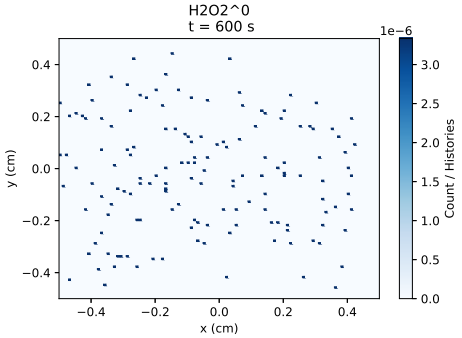

Figure 10: Histogram with $\kappa = 2.3 \cdot 10^{-2}$ s^{-1}.

Figure 11: Spatial distribution of H_2O_2 at 10 min.

For the lowest κ (Figure 9), we observe spatial homogeneity in H_2O_2 concentration and a relatively small loss of H_2O_2, comparing with pure free diffusion ($\kappa = 0$ s^{-1}, Figure 8). For $\kappa = 10^{-2}$ s^{-1}, little H_2O_2 survives (Figure 9). In any case, we lose all H_2O_2 at the hour scale (image not shown) required in our experiments (Figure 1). However, a lower κ may be justified as we will see.

Other than the choice of κ, there are two problems to be addressed. First, this method is slow since it requires the sampling of four random numbers to transport each particle individually. Secondly, we are limited by the number of molecules generated in the simulation. Although one could artificially increase them due to the simplicity of the generated distributions, it would exacerbate the first problem.

3.2.2 Experimental estimation of κ

In [Wagner et al., 2013], they determined the rate constant per cell, K:

$$K = \kappa / \rho_{\text{cells}} \tag{5}$$

where ρ_{cells} is the density of cells in the volume considered for H_2O_2 diffusion. In this article, K is found to have values between $0.46 \cdot 10^{-12}$ and $10.4 \cdot 10^{-12}$ s^{-1} $cells^{-1}$ L for mammalian cells.

For our experiments, we used FaDU cells (not included in [Wagner et al., 2013]). We calculated the cell density to be $\rho_{\text{cells}} = 7 \cdot 10^7$ cells/L at the time of measurement, resulting in an estimated $\kappa = 10^{-6} - 10^{-4}$ s^{-1}.

3.2.3 Model for transport II

We implemented Fick's equation for $[H_2O_2]$ as in [Zhang et al., 2023], generalising their approach to two dimensions:

$$\frac{\partial [H_2O_2]}{\partial \tau} = D \nabla^2 [H_2O_2] - \kappa [H_2O_2] \tag{6}$$

where $[H_2O_2] = [H_2O_2](x, y, \tau)$ and $\nabla^2 = \frac{\partial^2}{\partial x^2} + \frac{\partial^2}{\partial y^2}$. We solve Equation 6 numerically using Euler's forward method, faster than Method I for small enough τ and with $[H_2O_2]$ tending to 0 only asymptotically.

The initial condition for $[H_2O_2](x, y, 0)$ represents a mock distribution of the three microbeams of 0.1 x 8 mm^2 used in our experiment (Figure 12). It was generated based on the results in Section 2.

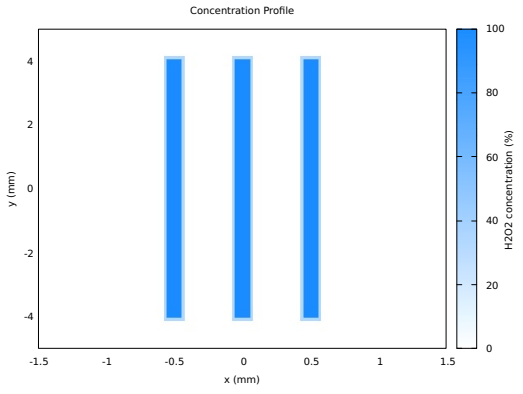

Figure 12: Mock distribution of H_2O_2 for the beam in the experiment.

In Figure 13, we show our results for $\kappa = 2.3 \cdot 10^{-3}$ s^{-1} and $\kappa = 2.3 \cdot 10^{-5}$ s^{-1}. After 10 min, we obtain around tree times more concentration for $\kappa = 2.3 \cdot 10^{-5}$ s^{-1} but the same spatial distribution.

In Figure 14, we see the evolution of H_2O_2 concentration at longer times for $\kappa = 2.3 \cdot 10^{-5}$ s^{-1}. We see that by 10 h, the H_2O_2 remaining is of the order of $\sim 10^{-43}$ %, showing that at the timescale needed, there is virtually no H_2O_2 left from the initial radiolysis contribution.

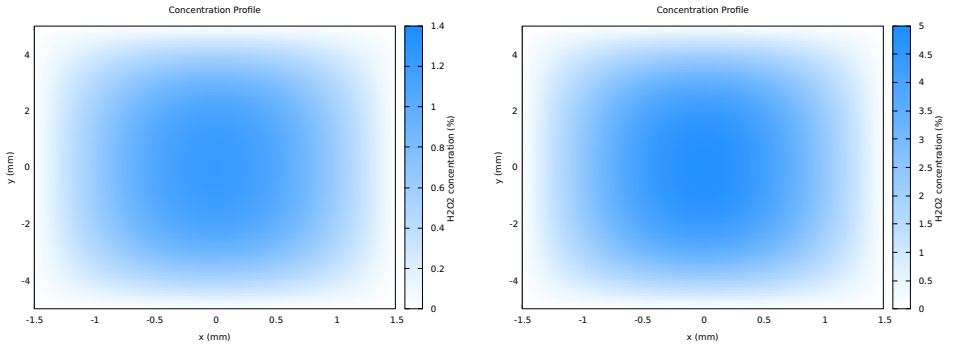

Figure 13: Comparison of H_2O_2 concentrations at 10 min for $\kappa = 2.3 \cdot 10^{-3}$ s^{-1} and $\kappa = 2.3 \cdot 10^{-5}$ s^{-1}.

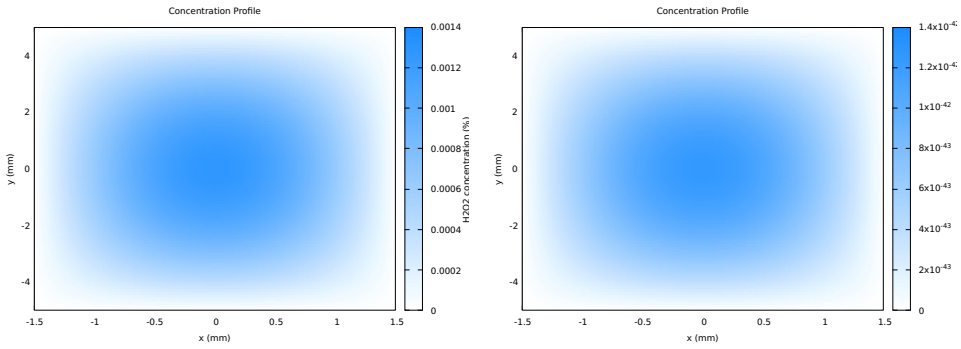

Figure 14: Comparison of H_2O_2 concentrations at 1 h and 10 h for $\kappa = 2.3 \cdot 10^{-5}$ s^{-1}.

We can conclude that H_2O_2 cannot be a signalling agent unless there is some producing mechanism balancing the scavenging processes.

4 Physical Limit of H_2O_2 Range

If we compare the SFRT beams creating the H_2O_2 distributions in Figures 2.1 and 12, we can expect their size and ctc to impact H_2O_2 achieving spatial homogeneity. If homogeneity of H_2O_2 is fast enough, it may trigger longer time effects [Decrock et al., 2017, Dal Bello et al., 2020]. Here, we will relate SFRT beam choice to possible differences in RIBE.

For the two examples in Figures 2.1 and 12, we see that it takes 550 s and 13 s for H_2O_2 to reach uniformity (see Figures 15 and 16). The initial distribution of Figure 16 was produced assuming the same behaviour as in the Monte Carlo generated Figure 2.1[4].

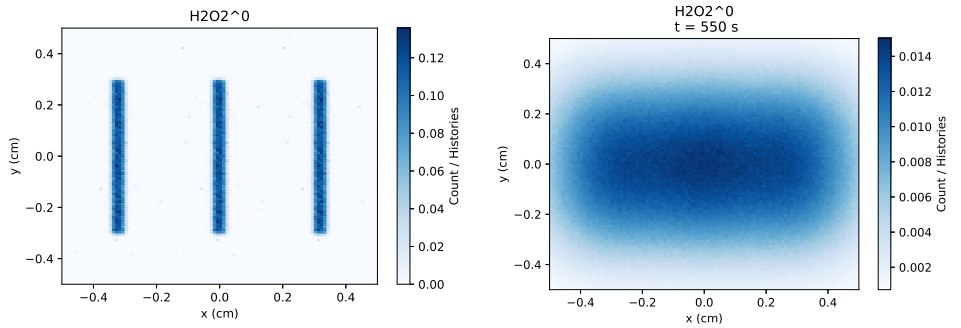

Figure 15: Comparison of H_2O_2 concentrations at 1 μs and 550s after free diffusion ($\kappa = 0$ s^{-1}) for the set-up in [Masilela, 2023] using Method I.

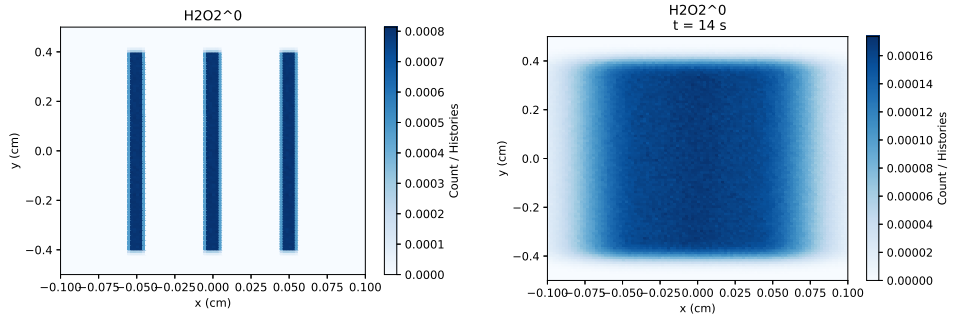

Figure 16: Comparison of H_2O_2 concentrations at 1 μs and 14 s after free diffusion ($\kappa = 0$ s^{-1}) for our experimental set-up using Method I.

Molecules diffuse following the Smolochowski equation, solved analyti-

[4]Figures 2.1 and 15-left are the same, reproduced here for convenience.

cally by the probability density function $p(r, \tau)$ [Karamitros et al., 2014]:

$$p(r, \tau) = \frac{4\pi r^2}{(4\pi D\tau)^{3/2}} \exp\left(-\frac{r^2}{4D\tau}\right) \tag{7}$$

where r is the distance travelled by a molecule in a time τ. The function $p(r, \tau)$ varies with τ but its shape is preserved at all times. An example at $\tau = 60$ s can be seen in Figure 17.

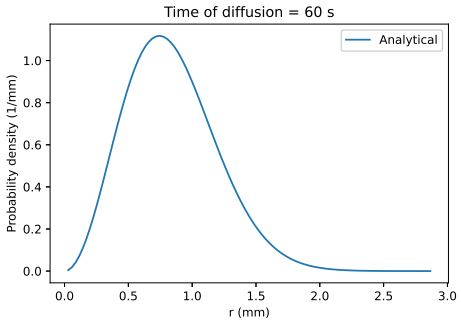

Figure 17: Smolochowski probability density function $\tau = 60$ s.

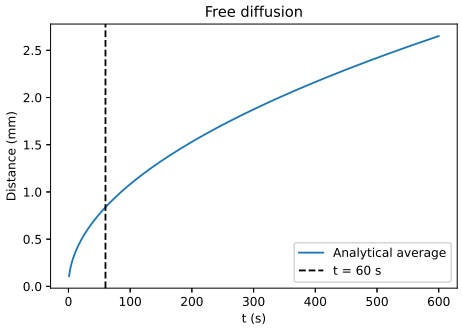

Figure 18: Average r as a function of τ.

We noticed that we achieve homogeneity in H_2O_2 concentration when $\bar{r}(\tau) \sim$ VW, where $\bar{r}(\tau) = \int r\, p(r, \tau)\, dr$ and VW is the valley width of the SFRT beam array[5]. The average distance travelled has a simple analytical expression, $\bar{r}(\tau) = 4\sqrt{\frac{D\tau}{\pi}}$, plotted in Figure 18. We also mark the line when $\tau = 60$ s to see that, at most, VWs of less than 1 mm will achieve homogeneity of H_2O_2 in that time.

This dependence may imply differences in the bystander effect of minibeams and microbeams. Nevertheless, this analysis assumed pure free diffusion in water, disregarding obstacles in biological media travel. Its conclusions can only be regarded as an upper limit.

[5]We tested the relationship in other beam arrays (see Appendix II).

5 Small RIBE Signals

Returning to the analysis of hour scale RIBE, there are experimental studies researching the role and concentration evolution of small RIBE signals in biological systems. Their main outcomes for H_2O_2 and Ca^{2+} are presented here.

5.1 H_2O_2 as RIBE signalling agent

The molecule of H_2O_2 has a short half-life, $t_{1/2}$, in biological systems. A study by [Orrico et al., 2022] showed $t_{1/2} \sim 34.5$ ms and others suggest similar values ([Wagner et al., 2013], references in Section 7.5 in [Masilela, 2023]). Alternatively, there are investigations reporting longer $t_{1/2}$, of the scale of seconds [Ledo et al., 2022]. Regardless, both observations exclude H_2O_2 as the main RIBE mediator in our experiments.

On the other hand, several studies propose that the initial concentration of H_2O_2 (and other radiolysis products) may generate long-lived radicals with $t_{1/2}$ of minutes ([Dringen and Hamprecht, 1997]) and hours [Gülden et al., 2010]. The cell type will most likely determine the specific mechanism for long-lived or continous short-lived radical production [Decrock et al., 2017]. We will briefly introduce one such mechanism involving Ca^{2+}.

5.2 Ca^{2+} Signalling in RIBE

Ca^{2+} is an important signalling agent, present in a number of processes [Berridge et al., 2000, Zong and Thompson, 2006, Du, 2008]. It is generated during all sorts of irradiations and produces transient or long-lasting increases in intracellular Ca^{2+}, within seconds to minutes after irradiation, indicating that changes in intracellular Ca^{2+} may represent an early response to radiation [Decrock et al., 2017].

Its role in the RIBE has been demonstrated in a variety of experiments [Decrock et al., 2017, Restier-Verlet et al., 2023], although responses in Ca^{2+} to radiation have not been observed in all cell lines investigated [Du, 2008].

Interstingly, there are several experiments evidencing the relationship between the generation of ROS, particularly H_2O_2 , and Ca^{2+} where adding/s-

cavenging Ca^{2+} increases/decreases the production of H_2O_2 and viceversa [Mukherjee and Chakraborty, 2019] [Ait-Aissa et al., 2022] [Nam et al., 2002] [Brandes and Wittig, 2022] [Gibhardt et al., 2015]. Furthermore, a mechanism for continuous generation of both Ca^{2+} and ROS after irradiation has been proposed (see caption of Figure 1 in [Decrock et al., 2017]), which could compensate for the short half-lives of ROS.

This self-amplifying loop can also affect ROS range when combined with the phenomenon of Ca^{2+} waves. Ca^{2+} concentration can describe a wave-like behaviour where an increase of Ca^{2+} in certain cells regions provokes a similar response in nearby areas. When the waves are simply ruled by diffusion, they are called passive waves. Ca^{2+} diffusion coefficient in water is of $7.8 \cdot 10^{-6}$ cm^2/s but decreases by a factor of a hundred have been observed in mammals [Morris and Krnjević, 1981]. In this case, Ca^{2+} behaviour would be similar to what we have seen for H_2O_2[6]. Nevertheless, active waves, where regeneration of Ca^{2+} is involved, allow for further reach [Leybaert and Sanderson, 2012]. There is a myriad of studies modelling both types [Sera and Kudo, 2020]. A combination of the higher range of Ca^{2+} active waves and the ability of Ca^{2+} to produce H_2O_2 may also imply a greater reach for H_2O_2.

However, to our knowledge, there are no experimental studies on the specific quantities of Ca^{2+} generated during irradiation, exploring the Ca^{2+} scavenging capacity of human organisms or the half-life of Ca^{2+} in the context of SFRT.

[6]Note that since we have the diffusion constant for Ca^{2+}, a similar study to Sections 3.2 and 4 can be easily done.

6 Cell Survival Models for the Bystander Effect

Unfortunately, there seems to be a lack of experimental data on the quantities of H_2O_2 and other RIBE signalling candidates produced after irradiation and their impact on the RIBE [Kundrát and Friedland, 2015]. Since our goal is to provide an explanation to the proton SFRT RIBE experiments developed in our group (Figure 1), we reviewed the cell-radiation models by:

1. [Matsuya et al., 2018]: an extension to the microdosimetric kinetic model in which RIBE are included is presented. The large number of parameters gives good reproduction of the data but its complexity difficults its application to other datasets.

2. [McMahon et al., 2013]: they show a model based on cell damage probability after photon irradiation. RIBE-induce damage is included through the action of an unkown signal concentration. Due to its simplicity, we will use it next.

6.1 Results of [McMahon et al., 2013]

The model covers the biological endpoints of a) cell survival and b) DNA damage; and the RIBE seen in i) uniform irradiation, ii) partial irradiation and iii) media transfer. The case of our experiments would be DNA damage and partial irradiation.

We first applied it to protons of the same cell line (H460) for the endpoint of cell survival and with uniform irradiation. We used the data in [Guan et al., 2015], focusing on the linear energy transfer (LET) range of the beam in our experiment (energies of 3 - 30 MeV, corresponding to 11.72 - 1.8 keV/μm). Since the model was initially developed for photons, we used the values for the relative biological effectiveness (RBE) given by [Guan et al., 2015]. As seen in Figures 19 and 20, this modified model agrees with the data.

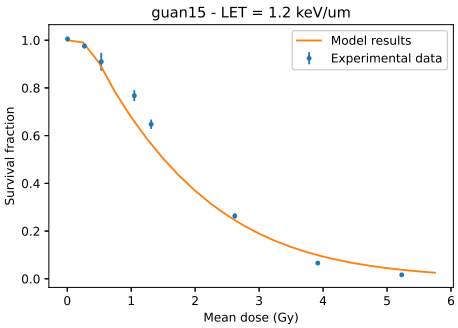

Figure 19: Results of [Guan et al., 2015] for protons of LET = 1.2 keV/μm.

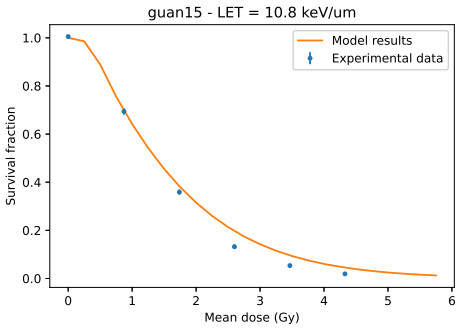

Figure 20: Results of [Guan et al., 2015] for protons of LET = 10.8 keV/μm.

The case considered here is simpler than our experiment. In order to apply the model, a set of steps could be:

- Find the model parameters for cell survival fraction experiments after photon irradiation of FaDu cells.
- Use the (now calibrated) model for cell DNA damage experiments after photon irradiation of FaDu cells.
- Use the model for cell survival fraction experiments after seamless proton irradiation of FaDu cells.
- Use the model for cell DNA damage experiments after seamless proton irradiation of FaDu cells.
- Use the model for cell survival fraction experiments after SFRT proton irradiation of H460 cells.
- Use the model for cell DNA damage experiments after SFRT proton irradiation of H460 cells.

7 Perspectives

We now present possible routes to follow from the work done here:

1. The methods in Section 2 can be applied to recreate the setup in our experiments. The faster independent reaction times (IRT) algorithm

[Ramos-Méndez et al., 2020] could substitute the step-by-step method used here.

2. The value for the diffusion coefficient of H_2O_2 in water was used in the extrapolation to biological systems. It is known that biological membranes prevent free diffusion [Möller et al., 2019] so a more refined diffusion coefficient is needed.

3. Several values for κ were proposed, being the ones based on [Wagner et al., 2013] the most varied and better justified. However, FaDu cells were not included and perhaps there are other published experiments covering them.

4. Following this line, it would be interesting to search for experiments examining the RIBE in FaDu cells specifically.

5. An analysis on Ca^{2+} diffusion towards the valleys starting from a mock distribution can be performed using the techniques in Section 3.2.

6. At the chemical level, it would be interesting to include the study of the homogenous stage using the (to be released) implementation of the Gillespie algorithm in TOPAS-nBio [D-Kondo et al., 2023].

7. If the steps proposed in Section 6.1 are fulfilled, a relationship of the concentration used in [McMahon et al., 2013] to the H_2O_2 concentration seen here can be established, providing insight into the model and perhaps reducing the number of fitting parameters.

8. Experimentally, a recent article [Autsavapromporn et al., 2023] has studied RIBE in proton SFRT. Specifically, it demostrated the mediation of NO and gap–junction intercellular communication in RIBE in A549 cells using specialised scavengers. Repeating our current experiments using H_2O_2 and Ca^{2+} scavengers may prove their involvement in our context.

8 Summary and Conclusions

During this research stay, we simulated the generation of free radicals and ROS in radiolysis with TOPAS-nBio in the context of proton SFRT, con-

firming that the spatial distribution of the chemicals coincides with that of the beam.

We have estimated the behaviour of H_2O_2 during the homogenous chemical stage and refined two mathematical models for the diffusion of H_2O_2 in the biological stage, concluding that H_2O_2 produced during radiolysis cannot mediate RIBE themselves unless other amplyfying mechanisms are involved, in agreement with previous data.

We have found a mechanistic justification for potential differences in RIBE between minibeams and microbeams and reviewed the experimental data on H_2O_2 and Ca^{2+}, presenting a mechanism for their mutual generation.

Finally, two models for RIBE on cells were examined. One was applied to uniform proton irradiation as an initial step towards a model for RIBE in proton SFRT.

References

[Ait-Aissa et al., 2022] Ait-Aissa, K., Koval, O. M., Lindsey, N. R., and Grumbach, I. M. (2022). Mitochondrial ca2+ uptake drives endothelial injury by radiation therapy. *Arterioscler. Thromb. Vasc. Biol.*, 42(9):1121–1136.

[Autsavapromporn et al., 2023] Autsavapromporn, N., Kobayashi, A., Liu, C., Duangya, A., Oikawa, M., Tengku Ahmad, T. A., and Konishi, T. (2023). Primary and secondary bystander effects of proton microbeam irradiation on human lung cancer cells under hypoxic conditions. *Biology*, 12(12):1485.

[Berridge et al., 2000] Berridge, M. J., Lipp, P., and Bootman, M. D. (2000). The versatility and universality of calcium signalling. *Nature Reviews Molecular Cell Biology*, 1(1):11–21.

[Brandes and Wittig, 2022] Brandes, R. P. and Wittig, I. (2022). Calcium-controlled reactive oxygen species afterburner perpetuates endothelial damage after radiation therapy. *Arteriosclerosis, Thrombosis, and Vascular Biology*, 42(9):1137–1138.

[D-Kondo et al., 2023] D-Kondo, J. N., Garcia-Garcia, O. R., LaVerne, J. A., Faddegon, B., Schuemann, J., Shin, W.-G., and Ramos-Méndez, J. (2023). An integrated monte carlo track-structure simulation framework for modeling inter and intra-track effects on homogenous chemistry. *Physics in Medicine ands Bissology*, 68(12):125008.

[Dal Bello et al., 2020] Dal Bello, R., Becher, T., Fuss, M. C., Krämer, M., and Seco, J. (2020). Proposal of a chemical mechanism for mini-beam and micro-beam efficacy. *Frontiers in Physics*, 8.

[Decrock et al., 2017] Decrock, E., Hoorelbeke, D., Ramadan, R., Delvaeye, T., De Bock, M., Wang, N., Krysko, D. V., Baatout, S., Bultynck, G., Aerts, A., Vinken, M., and Leybaert, L. (2017). Calcium, oxidative stress and connexin channels, a harmonious orchestra directing the response to radiotherapy treatment? *Biochimica et Biophysica Acta (BBA) - Molecular Cell Research*, 1864(6):1099–1120.

[Dilmanian et al., 2002] Dilmanian, F. A., Button, T. M., Le Duc, G., Zhong, N., Pena, L. A., Smith, J. A., Martinez, S. R., Bacarian, T., Tammam, J., Ren, B., Farmer, P. M., Kalef-Ezra, J., Micca, P. L., Nawrocky, M. M., Niederer, J. A., Recksiek, F. P., Fuchs, A., and Rosen, E. M. (2002). Response of rat intracranial 9L gliosarcoma to microbeam radiation therapy. *Neuro-Oncology*, 4(1):26–38.

[Dilmanian et al., 2003] Dilmanian, F. A., Morris, G. M., Zhong, N., Bacarian, T., Hainfeld, J. F., Kalef-Ezra, J., Brewington, L. J., Tammam, J., and Rosen, E. M. (2003). Murine emt-6 carcinoma: High therapeutic efficacy of microbeam radiation therapy. *Radiation Research*, 159(5):632–641.

[Dringen and Hamprecht, 1997] Dringen, R. and Hamprecht, B. (1997). Involvement of glutathione peroxidase and catalase in the disposal of exogenous hydrogen peroxide by cultured astroglial cells. *Brain Research*, 759(1):67–75.

[Du, 2008] Du, G. (2008). *A Calcium imaging setup at the single ion hit facility at GSI and its application to the investigation of Calcium response to ion irradiation in mammalian cells.* PhD Thesis, Technical University of Darmstadt.

[Edgar, 2016] Edgar, J. R. (2016). Q & a: What are exosomes, exactly? *BMC Biology*, 14(1).

[Gibhardt et al., 2015] Gibhardt, C. S., Roth, B., Schroeder, I., Fuck, S., Becker, P., Jakob, B., Fournier, C., Moroni, A., and Thiel, G. (2015). X-ray irradiation activates k+ channels via h2o2 signaling. *Scientific Reports*, 5(1).

[Gil et al., 2011] Gil, S., Sarun, S., Biete, A., Prezado, Y., and Sabés, M. (2011). Survival analysis of f98 glioma rat cells following minibeam or broad-beam synchrotron radiation therapy. *Radiation Oncology*, 6(1).

[Guan et al., 2015] Guan, F., Peeler, C., Bronk, L., Geng, C., Taleei, R., Randeniya, S., Ge, S., Mirkovic, D., Grosshans, D., Mohan, R., and Titt, U. (2015). Analysis of the track- and dose-averaged LET and LET spectra in proton therapy using the geant4 monte carlo code. *Medical Physics*, 42(11):6234–6247.

[Gülden et al., 2010] Gülden, M., Jess, A., Kammann, J., Maser, E., and Seibert, H. (2010). Cytotoxic potency of h2o2 in cell cultures: Impact of cell concentration and exposure time. *Free Radical Biology and Medicine*, 49(8):1298–1305.

[Karamitros et al., 2014] Karamitros, M., Luan, S., Bernal, M., Allison, J., Baldacchino, G., Davidkova, M., Francis, Z., Friedland, W., Ivantchenko, V., Ivantchenko, A., Mantero, A., Nieminem, P., Santin, G., Tran, H., Stepan, V., and Incerti, S. (2014). Diffusion-controlled reactions modeling in geant4-dna. *Journal of Computational Physics*, 274:841–882.

[Klammer et al., 2015] Klammer, H., Mladenov, E., Li, F., and Iliakis, G. (2015). Bystander effects as manifestation of intercellular communication of dna damage and of the cellular oxidative status. *Cancer Letters*, 356(1):58–71.

[Kundrát and Friedland, 2015] Kundrát, P. and Friedland, W. (2015). Mechanistic modelling of radiation-induced bystander effects: Figure 1. *Radiation Protection Dosimetry*, 166(1–4):148–151.

[Laissue et al., 2013] Laissue, J. A., Bartzsch, S., Blattmann, H., Bräuer-Krisch, E., Bravin, A., Dalléry, D., Djonov, V., Hanson, A. L., Hopewell,

J. W., Kaser-Hotz, B., Keyriläinen, J., Laissue, P. P., Miura, M., Serduc, R., Siegbahn, A. E., and Slatkin, D. N. (2013). Response of the rat spinal cord to x-ray microbeams. *Radiotherapy and Oncology*, 106(1):106–111.

[Ledo et al., 2022] Ledo, A., Fernandes, E., Salvador, A., Laranjinha, J., and Barbosa, R. (2022). In vivo hydrogen peroxide diffusivity in brain tissue supports volume signaling activity. *Redox Biology*, 50:102250.

[Leybaert and Sanderson, 2012] Leybaert, L. and Sanderson, M. J. (2012). Intercellular ca2+waves: Mechanisms and function. *Physiological Reviews*, 92(3):1359–1392.

[Marín et al., 2015] Marín, A., Martín, M., Liñán, O., Alvarenga, F., López, M., Fernández, L., Büchser, D., and Cerezo, L. (2015). Bystander effects and radiotherapy. *Reports of Practical Oncology; Radiotherapy*, 20(1):12–21.

[Masilela, 2023] Masilela, T. (2023). *In silico radiobiological investigations for the advancement of novel RT techniques.* PhD Thesis, Université Paris-Saclay.

[Matsuya et al., 2018] Matsuya, Y., Sasaki, K., Yoshii, Y., Okuyama, G., and Date, H. (2018). Integrated modelling of cell responses after irradiation for dna-targeted effects and non-targeted effects. *Scientific Reports*, 8(1).

[McMahon et al., 2013] McMahon, S. J., Butterworth, K. T., Trainor, C., McGarry, C. K., O'Sullivan, J. M., Schettino, G., Hounsell, A. R., and Prise, K. M. (2013). A kinetic-based model of radiation-induced intercellular signalling. *PLoS ONE*, 8(1):e54526.

[Miura et al., 2006] Miura, M., Blattmann, H., Bräuer-Krisch, E., Bravin, A., Hanson, A. L., Nawrocky, M. M., Micca, P. L., Slatkin, D. N., and Laissue, J. A. (2006). Radiosurgical palliation of aggressive murine sccvii squamous cell carcinomas using synchrotron-generated x-ray microbeams. *The British Journal of Radiology*, 79(937):71–75.

[Möller et al., 2019] Möller, M. N., Cuevasanta, E., Orrico, F., Lopez, A. C., Thomson, L., and Denicola, A. (2019). *Diffusion and Transport of Reactive Species Across Cell Membranes*, page 3–19. Springer International Publishing.

[Morris and Krnjević, 1981] Morris, M. E. and Krnjević, K. (1981). Slow diffusion of ca2+ in the rat's hippocampus. *Canadian Journal of Physiology and Pharmacology*, 59(9):1022–1025.

[Mukherjee and Chakraborty, 2019] Mukherjee, S. and Chakraborty, A. (2019). Radiation-induced bystander phenomenon: insight and implications in radiotherapy. *International Journal of Radiation Biology*, 95(3):243–263.

[Nam et al., 2002] Nam, S. H., Jung, S. Y., Yoo, C. M., Ahn, E. H., and Suh, C. K. (2002). H2o2enhances ca2+release from osteoblast internal stores. *Yonsei Medical Journal*, 43(2):229.

[Oppenheim, 2001] Oppenheim, J. J. (2001). Cytokines: Past, present, and future. *International Journal of Hematology*, 74(1):3–8.

[Orrico et al., 2022] Orrico, F., Lopez, A. C., Saliwonczyk, D., Acosta, C., Rodriguez-Grecco, I., Mouro-Chanteloup, I., Ostuni, M. A., Denicola, A., Thomson, L., and Möller, M. N. (2022). The permeability of human red blood cell membranes to hydrogen peroxide is independent of aquaporins. *Journal of Biological Chemistry*, 298(1):101503.

[Perl et al., 2012] Perl, J., Shin, J., Schümann, J., Faddegon, B., and Paganetti, H. (2012). TOPAS: An innovative proton monte carlo platform for research and clinical applications. *Medical Physics*, 39(11):6818–6837.

[Prezado, 2022] Prezado, Y. (2022). Divide and conquer: spatially fractionated radiation therapy. *Expert Reviews in Molecular Medicine*, 24.

[Prezado et al., 2018] Prezado, Y., Jouvion, G., Patriarca, A., Nauraye, C., Guardiola, C., Juchaux, M., Lamirault, C., Labiod, D., Jourdain, L., Sebrie, C., Dendale, R., Gonzalez, W., and Pouzoulet, F. (2018). Proton minibeam radiation therapy widens the therapeutic index for high-grade gliomas. *Scientific Reports*, 8(1).

[Ramos-Méndez et al., 2021] Ramos-Méndez, J., LaVerne, J. A., Domínguez-Kondo, N., Milligan, J., Štěpán, V., Stefanová, K., Perrot, Y., Villagrasa, C., Shin, W.-G., Incerti, S., McNamara, A., Paganetti, H., Perl, J., Schuemann, J., and Faddegon, B. (2021). Topas-nbio validation

for simulating water radiolysis and dna damage under low-let irradiation. *Physics in Medicine and Biology*, 66(17):175026.

[Ramos-Méndez et al., 2020] Ramos-Méndez, J., Shin, W., Karamitros, M., Domínguez-Kondo, J., Tran, N. H., Incerti, S., Villagrasa, C., Perrot, Y., Štěpán, V., Okada, S., Moreno-Barbosa, E., and Faddegon, B. (2020). Independent reaction times method in geant4-dna: Implementation and performance. *Medical Physics*, 47(11):5919–5930.

[Restier-Verlet et al., 2023] Restier-Verlet, J., Joubert, A., Ferlazzo, M. L., Granzotto, A., Sonzogni, L., Al-Choboq, J., El Nachef, L., Le Reun, E., Bourguignon, M., and Foray, N. (2023). X-rays-induced bystander effect consists in the formation of dna breaks in a calcium-dependent manner: Influence of the experimental procedure and the individual factor. *Biomolecules*, 13(3):542.

[Rivera et al., 2020] Rivera, J. N., Kierski, T. M., Kasoji, S. K., Abrantes, A. S., Dayton, P. A., and Chang, S. X. (2020). Conventional dose rate spatially-fractionated radiation therapy (sfrt) treatment response and its association with dosimetric parameters—a preclinical study in a fischer 344 rat model. *PLOS ONE*, 15(6):e0229053.

[Salvat, 2018] Salvat (2018). Penelope: A code system for monte carlo simulation of electron and photon transport. *OECD Nuclear Energy Agency*.

[Schuemann et al., 2018] Schuemann, J., McNamara, A. L., Ramos-Méndez, J., Perl, J., Held, K. D., Paganetti, H., Incerti, S., and Faddegon, B. (2018). Topas-nbio: An extension to the topas simulation toolkit for cellular and sub-cellular radiobiology. *Radiation Research*, 191(2):125.

[Sera and Kudo, 2020] Sera, T. and Kudo, S. (2020). Mathematical models for intra- and inter-cellular ca^{2+} wave propagations. *Journal of Biorheology*, 34(1):9–17.

[Shao et al., 2006] Shao, C., Lyng, F. M., Folkard, M., and Prise, K. M. (2006). Calcium fluxes modulate the radiation-induced bystander responses in targeted glioma and fibroblast cells. *Radiation Research*, 166(3):479–487.

[Shin, 2020] Shin, W.-G. (2020). *Development and application of the Geant4-DNA toolkit for the simulation of radiobiological effects at the sub-cellular scale*. PhD Thesis, Université de Bordeaux.

[Sotiropoulos et al., 2021] Sotiropoulos, M., Brisebard, E., Le Dudal, M., Jouvion, G., Juchaux, M., Crépin, D., Sebrie, C., Jourdain, L., Labiod, D., Lamirault, C., Pouzoulet, F., and Prezado, Y. (2021). X-rays minibeam radiation therapy at a conventional irradiator: Pilot evaluation in f98-glioma bearing rats and dose calculations in a human phantom. *Clinical and Translational Radiation Oncology*, 27:44–49.

[van der Sanden et al., 2010] van der Sanden, B., Bräuer-Krisch, E., Siegbahn, E. A., Ricard, C., Vial, J.-C., and Laissue, J. (2010). Tolerance of arteries to microplanar x-ray beams. *International Journal of Radiation Oncology*Biology*Physics*, 77(5):1545–1552.

[Wagner et al., 2013] Wagner, B. A., Witmer, J. R., van't Erve, T. J., and Buettner, G. R. (2013). An assay for the rate of removal of extracellular hydrogen peroxide by cells. *Redox Biology*, 1(1):210–217.

[Wang et al., 2018] Wang, R., Zhou, T., Liu, W., and Zuo, L. (2018). Molecular mechanism of bystander effects and related abscopal/cohort effects in cancer therapy. *Oncotarget*, 9(26):18637–18647.

[Zhang et al., 2023] Zhang, T., García-Calderón, D., Molina-Hernández, M., Leitão, J., Hesser, J., and Seco, J. (2023). A theoretical study of h2o2 as the surrogate of dose in minibeam radiotherapy, with a diffusion model considering radical removal process. *Medical Physics*, 50(8):5262–5272.

[Zong and Thompson, 2006] Zong, W.-X. and Thompson, C. B. (2006). Necrotic death as a cell fate. *Genes Dev.*, 20(1):1–15.

Appendix I

Model I's free diffusion tracking is based on the Smolochowski equation with diffusion coefficient, D, independent of the position and without external forces [Karamitros et al., 2014]:

$$\frac{\partial\, p(\mathbf{x},\tau)}{\partial \tau} = D\,\nabla^2 p(\mathbf{x},\tau) \tag{8}$$

where $p(\mathbf{x}, \tau)$ is the probability density function of the position of the molecule at a time τ. Our algorithm for free diffusion in which molecules are transported according to Equations 1-3 is based on the solution to this equation (Equation 7) [Karamitros et al., 2014]. In this Appendix we want to show that the algorithm of free diffusion plus the addition of a survival probability is a solution to Fick's equation (Equation 6).

For $\kappa = 0\ \mathrm{s}^{-1}$, Fick's equation and Equation 8 are the same. Their solutions are equivalent possibly up to a general normalisation factor since Equation 8 is an equation for a probability density function and Fick's equation is for a concentration, i.e. $[\mathrm{H_2O_2}](\mathbf{x}, \tau) = \alpha \cdot \mathbf{p}(\mathbf{x}, \tau)$ where $\alpha \in \mathbb{R}^+$.

Now, let $\phi(\mathbf{x}, \tau)$ be a solution to Equation 8, then $[\mathrm{H_2O_2}](\mathbf{x}, \tau) = \phi(\mathbf{x}, \tau) \cdot \mathbf{e}^{-\kappa\tau}$ is a solution to Fick's equation (Equation 6):

$$\frac{\partial\,[\mathrm{H_2O_2}]}{\partial\tau} = D\,\nabla^2[\mathrm{H_2O_2}] - \kappa\,[\mathrm{H_2O_2}] \tag{9}$$

$$\frac{\partial\ (\phi(\mathbf{x}, \tau) \cdot \mathbf{e}^{-\kappa\tau})}{\partial\tau} = D\,\nabla^2\left(\phi(\mathbf{x}, \tau) \cdot \mathbf{e}^{-\kappa\tau}\right) - \kappa\,\phi(\mathbf{x}, \tau) \cdot \mathbf{e}^{-\kappa\tau} \tag{10}$$

$$\frac{\partial\,\phi(\mathbf{x}, \tau)}{\partial\tau} \cdot e^{-\kappa\tau} - \kappa\,\phi(\mathbf{x}, \tau) \cdot \mathbf{e}^{-\kappa\tau} = D\,\nabla^2\phi(\mathbf{x}, \tau) \cdot \mathbf{e}^{-\kappa\tau} - \kappa\,\phi(\mathbf{x}, \tau) \cdot \mathbf{e}^{-\kappa\tau} \tag{11}$$

$$\frac{\partial\,\phi(\mathbf{x}, \tau)}{\partial\tau} = D\,\nabla^2\phi(\mathbf{x}, \tau) \tag{12}$$

where the last equation is Equation 8 and is solved by $\phi(\mathbf{x}, \tau)$ by definition. Hence our algorithm for Model I, which samples a solution of the form $\phi(\mathbf{x}, \tau) \cdot \mathbf{e}^{-\kappa\tau}$ is equivalent to solving Fick's equation numerically.

Appendix II

In this section, we present a continuation to the analysis done in Section 4 for different SFRT arrays used in publications[7]. In Table 1, we can see the VW and time taken for homogeneity, τ_h, of $\mathrm{H_2O_2}$. We see that generally $\bar{r}\,(\tau_h) \sim$ VW with the exception of [Rivera et al., 2020].

[7] Arrays retrieved from a review by J. McGarrigle

Reference	**VW (mm)**	τ_h **(s)**	$\bar{r}(\tau_h)$ (mm)
[Dilmanian et al., 2002]	0.073	0.75	0.09
[Laissue et al., 2013]	0.175	2.25	0.16
[Dilmanian et al., 2003]	0.21	4.5	0.23
[van der Sanden et al., 2010]	0.35	10	0.34
[Miura et al., 2006]	0.13	2.1	0.16
[Prezado et al., 2018]	2.1	500	2.42
[Sotiropoulos et al., 2021]	0.7	110	1
[Rivera et al., 2020]	1.6	550	2.54
[Gil et al., 2011]	0.6	60	0.84

Table 1: Published valley widths and its corresponding τ_h and $\bar{r}(\tau_h)$.